
Validating Climate Models with Spherical Convolutional Wasserstein Distance

Robert C. Garrett¹ Trevor Harris² Bo Li¹ Zhuo Wang³

Abstract

The validation of global climate models is crucial to ensure the accuracy and efficacy of model output. We introduce the spherical convolutional Wasserstein distance to more comprehensively measure differences between climate models and reanalysis data. This new similarity measure accounts for spatial variability using convolutional projections and quantifies local differences in the distribution of climate variables. We apply this method to evaluate the historical model outputs of the Coupled Model Intercomparison Project (CMIP) members by comparing them to observational and reanalysis data products. Additionally, we investigate the progression from CMIP phase 5 to phase 6 and find modest improvements in the phase 6 models regarding their ability to produce realistic climatologies.

1. Introduction

Climate Model Validation General Circulation Models, or climate models, are mathematical representations of the climate system that describe interactions between matter and energy through the ocean, atmosphere, and land (Washington & Parkinson, 2005). Climate models are the primary tool for investigating the response of the climate system to changes in forcing, such as increases in CO₂, and projecting future climate states (Flato et al., 2014). To assess the plausibility of climate models, climate scientists compare output from model simulations against observational data (Rood, 2019). This comparison is the focus of climate model validation techniques for ensuring that climate models capture the dynamics of the climate system (Roca et al., 2021).

The Coupled Model Intercomparison Project (CMIP) was initiated in 1995 as a comprehensive and systematic program for assessing climate models against each other and observational data (Eyring et al., 2016). Each model in

CMIP participates in a wide variety of experiments such as performing a historical simulation, a pre-industrial control simulation, and various simulations representing different scenarios for CO₂ emissions (Eyring et al., 2016). Because historical simulations coincide with observational measurements, we can compare each model’s synthetic climate distribution to the distribution of observational or quasi-observational data products (Raäisaänen, 2007), to assess their reconstructive skill. For complete spatial coverage we compare against reanalysis data, a blend of observations and short-range weather forecasts through data assimilation (Bengtsson et al., 2004). This has become one popular climate model validation method (Flato et al., 2014).

Previous approaches Many statistical and machine learning-based methods have been applied to assess climate model output against reanalysis fields. The most common approach is to compute the L_2 distance, or root mean square error (RMSE), between different features of the climate model output and the reanalysis field (Li et al., 2021; Zamani et al., 2020; Karim et al., 2020; Ayugi et al., 2021). RMSE provides a direct measure of the differences between two climate fields but does not take into account randomness of data, so we should use it with caution in evaluating climate models. Another approach, which is invariant to bias, is to compute measures of correlation between climate model output and reanalysis fields (Zhao et al., 2021; Zamani et al., 2020; Karim et al., 2020; Ayugi et al., 2021).

More comprehensive approaches employ techniques for random processes to compare two spatial fields. For example, Shen et al. (2002) and Cressie et al. (2008) use the wavelet decomposition to compare the spatial-frequency content of two fields. Hering & Genton (2011) measures the loss differential between models of spatial processes, Lund & Li (2009) and Li & Smerdon (2012) compare the first and second moments of two random processes, and Yun et al. (2022) identifies local differences in the mean and dependency structure between two spatiotemporal climate fields. Functional data analysis techniques have been introduced to compare spatial and spatiotemporal random fields, considering the random fields as continuous functions. Many of these approaches compare the underlying mean functions from two sets of functional data (Zhang & Chen, 2007; Horváth et al., 2013; Staicu et al., 2014). Other approaches include the second-order structure in the comparison (Zhang

¹Department of Statistics, University of Illinois at Urbana-Champaign, Urbana, IL, USA ²Department of Statistics, Texas A&M University, College Station, TX, USA ³Department of Atmospheric Sciences, University of Illinois at Urbana-Champaign, Urbana, IL, USA. Correspondence to: Robert Garrett <rcg4@illinois.edu>.

& Shao, 2015; Li et al., 2016), or compare the distributions of two spatial random processes (Harris et al., 2021).

Since climate models aim to mimic the real climate which is the underlying pattern of weather, directly assessing the distributional differences between the modeled and observed data seems a more thorough approach to evaluating climate models. Vissio et al. (2020) proposed to use the Wasserstein distance (WD), a popular metric for comparing probability distributions (Villani & Villani, 2009), for such purpose. The WD can be intractable or even impossible to calculate between high-dimensional distributions (Kolouri et al., 2019), so Vissio et al. (2020) first converts each climate field to a single spatial mean and then only compares the distribution of spatial means. However, this dimension reduction puts their method at the risk of missing important spatial variability information, and consequently failing to accurately distinguish two climate fields that are different.

Recent contributions in the Machine Learning literature seek to compare multivariate distributions using many features while leveraging the efficiency of the one-dimensional WD (Vallender, 1974). The sliced WD (Bonneel et al., 2015) compares random projections of distributions on \mathbb{R}^n , and the generalized sliced WD (Kolouri et al., 2019) extends this to a broader class of projections. The convolutional sliced WD (Nguyen & Ho, 2022) compares distributions of discrete square images in the space $\mathbb{R}^{n \times n}$, accounting for the spatial structure using kernel convolutions. However, spatial fields from climate models are defined on a spherical domain, making them incompatible with the vectorized/square nature of these distances. The spherical sliced WD (Bonet et al., 2022) can compare distributions of spatial point processes over a sphere, such as locations of natural disasters and extreme weather events, but cannot be used for smooth fields such as daily temperature and precipitation.

Our proposal We propose the functional sliced WD as a generalization of sliced WD to distributions of functional data. To create a tailored tool for climate model evaluation, we define the Spherical Convolutional Wasserstein distance (SCWD) as a special case of the functional sliced WD for functions on the unit sphere \mathbb{S}^2 , the manifold on which latitude-longitude coordinates are defined. SCWD creates slices containing a small region of spatial fields to characterize local differences in the distribution of climate variables, which are further integrated into a single measure for global differences. Compared to the spatial mean-based WD from Vissio et al. (2020), SCWD accounts for spatial features while maintaining the modest computation for univariate WD when comparing climate models against reanalysis data, resulting in a comprehensive and more robust evaluation. We apply SCWD to rank climate models and assess the progression of the new CMIP era with respect to daily average surface temperature and daily total precipitation.

2. Preliminaries

We consider the problem of comparing two probability distributions P and Q . Each distribution is a member of $\mathcal{P}(\Omega)$, the set of Borel probability measures on some sample space, Ω . In our application, we treat climate fields as functional data (Wang et al., 2016) over some spatial domain \mathcal{S} , thus we often assume Ω is a space of functions. Our sample space of interest is $L^2(\mathcal{S})$, the set of square integrable functions from $\mathcal{S} \rightarrow \mathbb{R}$ where \mathcal{S} is a compact subset of \mathbb{R}^n . Because CMIP model outputs are available at a global scale, we consider the spatial domain to be the unit sphere \mathbb{S}^2 , the space over which latitude and longitude coordinates are assigned to the Earth’s surface. In fact, the function space $L^2(\mathbb{S}^2)$ has been previously considered for modeling climate fields (Heaton et al., 2014). To compare two functional data distributions P and Q , we define a distance function $D(P, Q)$ to act as a similarity measure.

Comparing Distributions of Functions Comparisons for distributions of functions in $L^2(\mathcal{S})$ have been studied for specific cases of \mathcal{S} (Hall & Van Keilegom, 2007; Bugni & Horowitz, 2021; Pomann et al., 2016; Harris et al., 2021), but none of these have focused on $L^2(\mathbb{S}^2)$. The mathematical properties of probability measures in $\mathcal{P}(L^2(\mathcal{S}))$ have been studied before (Gijbels & Nagy, 2017; Kim, 2006), but it is challenging to calculate distances such as the WD in this space without additional assumptions (Li & Ma, 2020). To define a similarity measure for distributions in $\mathcal{P}(L^2(\mathcal{S}))$, we build on the theory of the sliced WD and its various extensions, which have only been defined for distributions of finite-dimensional data.

Sliced WD Given a Borel function $\pi : \Omega \rightarrow \mathbb{R}$, the push-forward of P under π is a valid distribution in $\mathcal{P}(\mathbb{R})$ defined as $\pi \# P(B) = P(\pi^{-1}(B))$ for all Borel sets B in \mathbb{R} . The r -th order sliced WD (Bonneel et al., 2015) between $P, Q \in \mathcal{P}(\mathbb{R}^n)$ is a metric defined as the mean of the ordinary WD over univariate pushforwards:

$$SW_r(P, Q) = \left(\int_{\mathbb{S}^{n-1}} W_r(\pi_\theta \# P, \pi_\theta \# Q)^r d\theta \right)^{1/r}, \quad (1)$$

where $\pi_\theta(x) = x^T \theta$ for $x \in \mathbb{R}^n$ and $\theta \in \mathbb{S}^{n-1}$. We call π_θ the slicing function because it produces one-dimensional “slices” of the data using projection matrices. Because $\pi_\theta \# P$ and $\pi_\theta \# Q$ are valid distributions in $\mathcal{P}(\mathbb{R})$, the WD inside the integral can be calculated with the commonly used analytical form for univariate measures (Vallender, 1974). Given two samples $X \sim P$ and $Y \sim Q$ we can approximate $SW_r(P, Q)$ using the following Monte Carlo integral:

$$\left(\frac{1}{m} \sum_{i=1}^m \int_0^1 \left| \hat{F}_{X^T \theta_i}^{-1}(q) - \hat{F}_{Y^T \theta_i}^{-1}(q) \right|^r dq \right)^{1/r}, \quad (2)$$

where $\theta_1, \dots, \theta_m$ is a random sample of projections from \mathbb{S}^{n-1} and $\hat{F}_{X^T\theta_i}^{-1}, \hat{F}_{Y^T\theta_i}^{-1}$ are the empirical quantile functions of $X^T\theta_i$ and $Y^T\theta_i$, respectively, for $i = 1, \dots, m$.

Generalized Sliced WD The generalized sliced WD (Kolouri et al., 2019) replaces π_θ with a more general class of slicing functions, denoted as g_θ . Because of this increased flexibility, the generalized sliced WD is a pseudometric rather than a metric except for specific cases of g_θ (Kolouri et al., 2019). For a given use case, the utility and metric properties of the generalized sliced WD are therefore determined by the choice of slicing function. Slicing functions can be chosen via optimization, estimated using neural networks, or specified by the researcher to isolate features of interest (Kolouri et al., 2019). The last option is desirable for our application, allowing the slices to be restricted to spatial features of interest to climate modelers.

However, the generalized sliced WD is defined between distributions of data in \mathbb{R}^n , a space that is not suitable for distributions of spatial fields. Climate fields could be coerced to vectors in \mathbb{R}^n to be made compatible with the generalized sliced WD. However, this would result in a loss of the inherent spatial structure, making it challenging to specify a slicing function that can handle considerations such as area weighting and spatial correlations.

Convolution Sliced WD The convolution sliced WD (Nguyen & Ho, 2022) represents images as matrices in the space $\mathbb{R}^{n \times n}$. The slicing function is replaced with kernel convolutions, or possibly a sequence of kernel convolutions, of $d \times d$ pixels for $d \in \mathbb{N}$. The kernel aggregates nearby locations to isolate local features, which could provide useful information to climate modelers. However, when climate fields are represented on a rectangular grid, the geographic area represented by each grid cell varies drastically between latitudes due to the non-Euclidean structure. Thus, a $d \times d$ pixel kernel will cover different sizes and shapes of geographic areas depending on location. For our application, the kernel radius should therefore be defined using geographic distance, not pixels.

3. Methods

We introduce the functional sliced WD framework which extends the flexible slicing process from the generalized sliced WD to the infinite-dimensional case of functions in $L^2(\mathcal{S})$. We focus on the special case of $L^2(\mathbb{S}^2)$, which we call the spherical convolutional WD (SCWD), for our climate model validation application. SCWD adapts the kernel convolution-based slicing idea of the convolutional sliced WD (Nguyen & Ho, 2022) to a continuous setting while accounting for the non-euclidean structure of climate fields realized over the Earth’s surface.

3.1. Functional Sliced Wasserstein Distance

In general it is not possible to analytically characterize distributions in $\mathcal{P}(L^2(\mathcal{S}))$ and there are no closed form solutions for computing the Wasserstein distance. However, it is possible to slice elements of $L^2(\mathcal{S})$, meaning we can leverage the analytical form of the one-dimensional WD to define a computable sliced WD. We first extend the convolution slicer from Nguyen & Ho (2022) to the functional data case, allowing us to project functions in $L^2(\mathcal{S})$ to values in \mathbb{R} while preserving local spatial information.

Definition 3.1 (Convolution Slicer). Let \mathcal{S} be a compact subset of \mathbb{R}^n , $s \in \mathcal{S}$, and k , called the kernel function, be a continuous function from $\mathcal{S} \times \mathcal{S} \rightarrow [0, \infty)$. We define the convolution slicer $c_s(f)$, a linear operator from $f \in L^2(\mathcal{S}) \rightarrow \mathbb{R}$, as follows:

$$c_s(f) = \int_{\mathcal{S}} f(u)k(s, u)du.$$

Since location $s \in \mathcal{S}$ is fixed, $k(s, u)$ is a continuous function from $u \in \mathcal{S} \rightarrow \mathbb{R}$. Because \mathcal{S} is compact, it follows that $k(s, u)$ is bounded and thus $k(s, u) \in L^2(\mathcal{S})$. So, by Hölder’s inequality, $c_s(f)$ is a bounded linear operator from $L^2(\mathcal{S}) \rightarrow \mathbb{R}$. Bounded linear operators are also continuous (Stein & Shakarchi, 2011), so $c_s(f)$ is a continuous linear operator and, therefore, Borel measurable. Thus, for any measure $P \in \mathcal{P}(L^2(\mathcal{S}))$, the pushforward $c_s\#P$ is a valid measure in $\mathcal{P}(\mathbb{R})$. Thus, we can define a functional sliced WD between distributions in $\mathcal{P}(L^2(\mathcal{S}))$ as follows:

Definition 3.2 (Functional Sliced WD). Let \mathcal{S} be a compact subset of \mathbb{R}^n , $r \geq 1$, and $P, Q \in \mathcal{P}(L^2(\mathcal{S}))$. Let c_s be an operator satisfying Definition 3.1. We define the (r -th order) functional sliced WD between P and Q as follows:

$$FSW_r(P, Q) = \left(\int_{\mathcal{S}} W_r(c_s\#P, c_s\#Q)^r ds \right)^{1/r}$$

where W_r is the Wasserstein metric on $\mathcal{P}(\mathbb{R})$.

Because $c_s\#P$ and $c_s\#Q$ are valid univariate probability measures, the analytical form of the univariate WD can be applied for efficient calculations. We introduce theoretical properties for the functional sliced WD in Theorem 3.3

Theorem 3.3. For all compact subsets $\mathcal{S} \subset \mathbb{R}^n$, FSW_r is a pseudometric on $\mathcal{P}(\mathcal{F}_{\mathcal{S}})$ and maintains the r -convexity property of the ordinary W_r metric.

Proof of Theorem 3.3 is provided in Appendix A. It is unknown if the final positivity property of a metric is satisfied. Proof of this property would require an invertible Radon-like transformation to be defined for probability measures in $\mathcal{P}(L^2(\mathcal{S}))$. Therefore, as with the generalized sliced WD, it is up to the researcher to specify an appropriate kernel

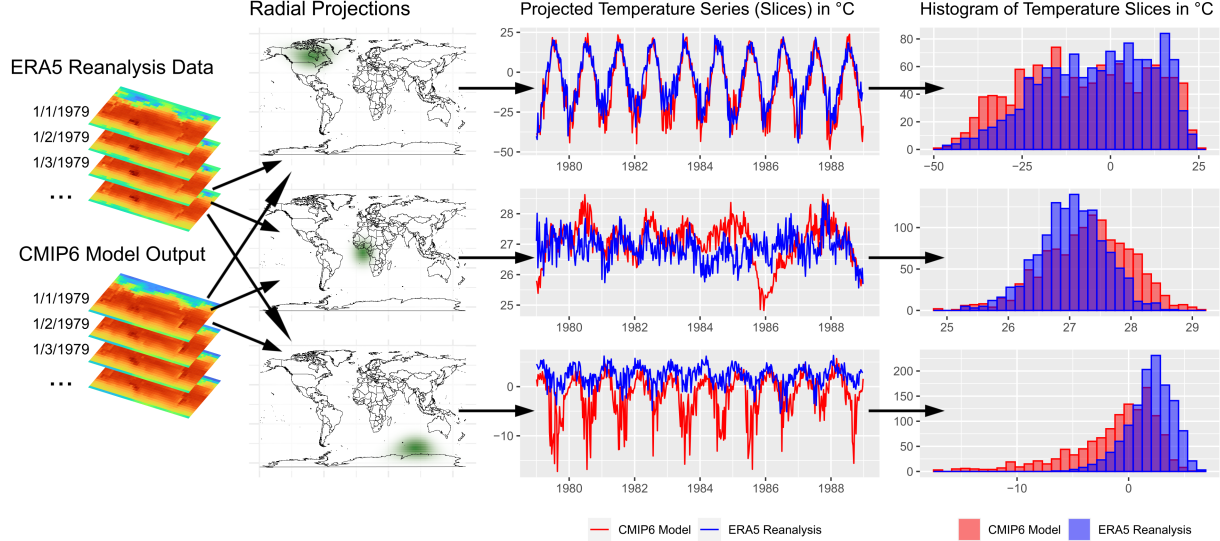


Figure 1. Diagram representing the calculation of SCWD between two distributions of daily mean surface temperature fields from ERA5 and a CMIP6 model. For each day, radial projections are computed through kernel convolutions, represented here at three different locations. The resulting projections, called slices, summarise the local climate conditions in each dataset. The slices for each day are viewed as a sample from the marginal distribution at each location, represented here as histograms. SCWD is calculated as a global mean over the univariate WD between each pair of local distributions.

function over the domain of interest. We provide such a choice for our application and give theoretical justification in Section 3.2.

3.2. Spherical Convolutional Wasserstein Distance

For our application to climate model validation, we specify the spatial domain \mathcal{S} to be the unit sphere \mathbb{S}^2 , the space over which latitude-longitude coordinates are assigned to locations on the Earth. To preserve local spatial information, we specify the slicing function to be a radial kernel function. We introduce the spherical convolutional WD (SCWD) as a specific case of the functional sliced WD:

Definition 3.4 (Spherical Convolutional WD). Let $P, Q \in \mathcal{P}(L^2(\mathbb{S}^2))$ and $r \geq 1$. We define the (r -th order) SCWD between P and Q as follows:

$$SCW_r(P, Q) = \left(\int_{\mathbb{S}^2} W_r(\omega_s \# P, \omega_s \# Q)^r ds \right)^{1/r},$$

where ω_s is a convolution slicer that satisfies Definition 3.1 with associated radial kernel function $\phi(s, u)$:

$$\omega_s(f) = \int_{\mathbb{S}^2} f(u) \phi(s, u) du.$$

Because ϕ is a radial kernel function, ω_s aggregates local information and the resulting pushforward measures $\omega_s \# P$ and $\omega_s \# Q$ represent the local distribution around each location s . SCWD is therefore calculated as the global mean of

the WD between local distributions at each location. The local WD values can be recorded and later visualized as a map to pinpoint regions with higher or lower similarity. Figure 1 demonstrates the process for calculating SCWD between two distributions of surface temperature fields, and details on the implementation are provided in Appendix B. Similar to the sliced WD approximation (see equation 2), the computation uses Monte Carlo integration, with the outside sum replaced by a strided convolution over the sphere.

Choice of Kernel In our analysis, we specify the kernel function centered to be $\phi(|s - u|; l)$, where $|s - u|$ is the chordal distance between locations s and u and ϕ is the Wendland kernel function used in Nychka et al. (2015):

$$\phi(d; l) = \begin{cases} (1 - d)^6 (35d^2 + 18d + 3) / 3 & d \leq l, \\ 0 & d > l, \end{cases} \quad (3)$$

with range parameter $l > 0$ determining the radius over which the kernel is nonzero. The Wendland kernel meets the continuity assumption in Definition 3.1 and is also compact, which enables efficient sparse computations for our analysis.

Positive definite kernels, such as the Wendland kernel for l less than the diameter (Hubbert & Jäger, 2023), allow us to retain full spatial information via the spectral density. This is because the convolution theorem on \mathbb{S}^2 (Driscoll & Healy, 1994) gives an injective correspondence between the spectral density of a function $f \in L^2(\mathbb{S}^2)$ and the spectral density of the convolution $(f * k)(s) = \int_{\mathbb{S}^2} f(u) k(s, u) du$

when k is positive definite. Note that as $l \rightarrow \infty$, the Wendland kernel converges to the flat kernel $\phi(d; \infty) = 1$, resulting in a SCWD where every slice is the global mean. In this case, the SCWD will be equal to the global mean-based WD from [Vissio et al. \(2020\)](#), leading to a complete loss of spatial variability information. In our analysis, we ensure a positive definite kernel by specifying l to be less than the diameter of the Earth (about 12,750 km). We study the sensitivity of our results to this parameter in Section 4.4.

4. Climate Model Validation

We consider climate model outputs from the Coupled Model Intercomparison Project (CMIP) historical experiment phases 5 and 6. We focus on daily average near-surface (2m) temperature in degrees Celsius and daily total precipitation in mm. The CMIP6 historical simulations are organized by ensembles, each of which is distinguished with an `ripf` identifier (`rip` for CMIP5), representing realization, initialization, physics, and forcings of the model, respectively ([Eyring et al., 2016](#)). We obtain 46 CMIP6 model outputs with the `r1i1p1f1` ID and 33 CMIP5 model outputs with the `r1i1p1` ID. Output was obtained either at the daily frequency or aggregated from 3-hourly data. At the time of writing, two of the 79 total models did not have output available at a suitable frequency for surface temperature. All 79 models had output available for total precipitation.

To serve as references for climate model evaluation, we collect the European Centre for Medium-Range Weather Forecasts (ECMWF) Reanalysis 5th Generation (ERA5) ([Hersbach et al., 2020](#)) as well as the Reanalysis-2 data from the National Centers for Environmental Protection (NCEP) ([Kanamitsu et al., 2002](#)) reanalysis datasets. Both datasets were obtained for surface temperature and total precipitation at a daily frequency. Due to known issues with reanalysis data for precipitation ([Tapiador et al., 2017](#)), we obtain observations from the National Centers for Environmental Information (NCEI) Global Precipitation Climatology Project (GPCP) Daily Precipitation Analysis Climate Data Record ([Huffman et al., 2001](#); [Adler et al., 2020](#)) as an additional reference for precipitation only.

The historical time periods for each climate variable were chosen to maximize the available model outputs and reference datasets. For surface temperature, a common time period of January 1, 1979 to November 30th, 2005 was collected for each CMIP output and reanalysis dataset. For total precipitation, we restrict the time period to October 1, 1996 to November 30th, 2005 to accommodate the first available day of observations in the GPCP dataset. Each data product represents the climate variables on a different latitude-longitude grid, which varies in size and structure. See Appendix C for full details on the spatial resolution and availability of temperature/precipitation for each dataset.

4.1. Evaluation of CMIP6 Models

To evaluate the skill of CMIP6 models in characterizing local climate distributions, we compute the SCWD between each model output and the observed/reanalysis datasets. Smaller SCWD values indicate more similarity between local distributions in a model output and the reference dataset. We do not expect perfect agreement between models and historical data, so, similar to [Vissio et al. \(2020\)](#), we additionally calculate SCWD between the reference datasets as a baseline for comparison. All SCWD calculations in this section are performed using the Wendland kernel with range parameter of 1,000km for slicing.

We select the ERA5 Reanalysis as our reference dataset for (2m) surface temperature due to its high spatial resolution. We calculate distances from each surface temperature model output in our CMIP5 and CMIP6 ensembles to ERA5. In addition, we calculate the SCWD between ERA5 and the NCEP Reanalysis to compare the variability between reanalysis datasets to the variability between models and reanalysis. For total precipitation, we select the GPCP observational data as our reference dataset. We calculate distances from each total precipitation model output in our CMIP5 and CMIP6 ensembles to GPCP. We include SCWD calculations from GPCP to both ERA5 and NCEP for comparison, with the secondary goal of assessing the accuracy of each reanalysis in faithfully filling gaps in observed precipitation measurements. Full details on the SCWD rankings can be seen in Tables 2 and 3 in Appendix D. Here, we focus on the results for CMIP6, and Figure 2 provides the SCWD from each CMIP6 model output to the ERA5 surface temperature field and GPCP total precipitation field.

Surface Temperature For surface temperature, NCEP has a lower SCWD to ERA5 than all CMIP models. This is not a surprise: both ERA5 and NCEP are based on observations, so we expect their temperature distributions to be similar in most regions. Among the model outputs, many models have a SCWD to ERA5 similar to that of NCEP. In particular, AWI-CM-1-1-MR from the Alfred Wegener Institute and MPI-ESM1-2-HR from the Max Planck Institute have the lowest SCWD for surface temperature, with a few models close behind.

Total Precipitation Compared to surface temperature, NCEP no longer has a lower SCWD to GPCP than the CMIP6 models. Instead, the ERA5 total precipitation field, which has the lowest SCWD to GPCP, serves as a better baseline for comparison. Deficiencies of precipitation from reanalysis have been reported in previous studies ([Janowiak et al., 1998](#)). In brevity, precipitation is sensitive to model physics and is not strongly constrained by observations via data assimilation. The low SCWD of ERA5 can likely be attributed to the high model resolution and more advanced model physics and data assimilation system compared to

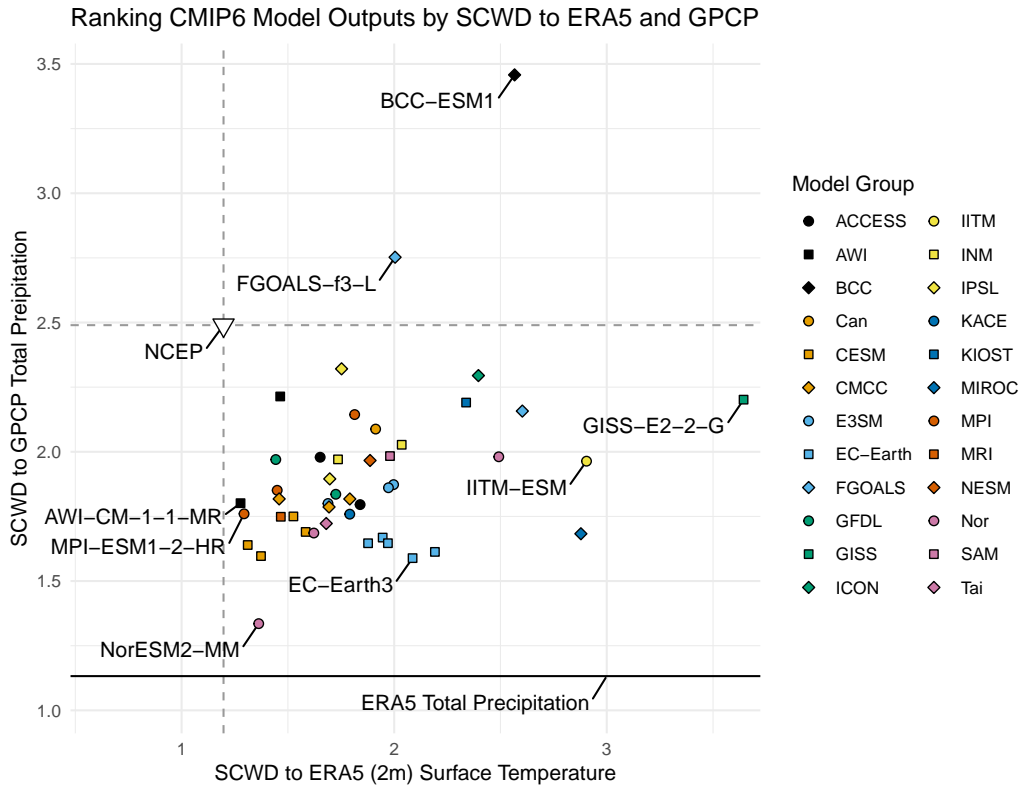


Figure 2. Ranking CMIP6 model outputs using SCWD. Each model output is represented by a point on the scatter plot and models from the same group share the color and shape. The x-axis and y-axis values represent each model’s SCWD to the ERA5 surface temperature and GPCP total precipitation fields, respectively. The NCEP reanalysis is included as a blank triangle with dashed lines representing the SCWD to ERA5 and GPCP. The SCWD from the ERA5 total precipitation field to GPCP is represented as a solid line.

NCEP. Among the CMIP6 models, the Norwegian Climate Centre NorESM2-MM model output stands out with the lowest SCWD to GPCP by a relatively wide margin. The EC-Earth3 and CESM model outputs also form clusters with low SCWD values for precipitation.

No single model has the lowest SCWD value for both surface temperature and total precipitation, but NorESM2-MM seems to have the best balance of low distances for each variable and is not far off from the intersection of the lines for our reference datasets. Similarly, no model has the highest SCWD value for both climate variables. The GISS-E2-2-G model from NASA’s Goddard Institute for Space Studies is a distinct outlier with a high surface temperature SCWD to ERA5, and the Beijing Climate Center BCC-ESM1 model is an outlier in terms of high SCWD to GPCP. We investigate these high SCWD values in Section 4.2.

4.2. Spatial Comparisons

Because SCWD is calculated as a global mean of local WD values, we can investigate the geographic sources of these outlying high SCWD values. Figure 3 provides a spatial breakdown of the local WD values obtained when calcu-

lating SCWD for surface temperature between ERA5 and AWI-CM-1-1-MR as well as ERA5 and GISS-E2-2-G, the models with the lowest and highest SCWD to ERA5, respectively. Overall, both maps seem smooth or continuous in space, with little variation between neighboring locations in most cases. For the map between AWI-CM-1-1-MR and ERA5, the local WD values are relatively low everywhere, with regions of slightly higher values near the poles and mountains. Compared to AWI-CM-1-1-MR, the GISS-E2-2-G model has similarly low WD values in the tropics. However, closer to the poles, the local WD values begin to increase. In particular, the Arctic region has extremely high WD values relative to the rest of the Earth. This is indicative of the previously documented winter cool bias in the Arctic region for GISS-E2-2-G (Kelley et al., 2020).

Similar maps are provided for the NorESM2-MM and BCC-ESM1 outputs compared to GPCP total precipitation. Overall, both maps are less smooth than the surface temperature maps, potentially due to the more localized nature of precipitation. Looking at both models, the higher values of SCWD near the equator in the Pacific and Atlantic oceans may be related to the double-Intertropical Convergence Zone problem

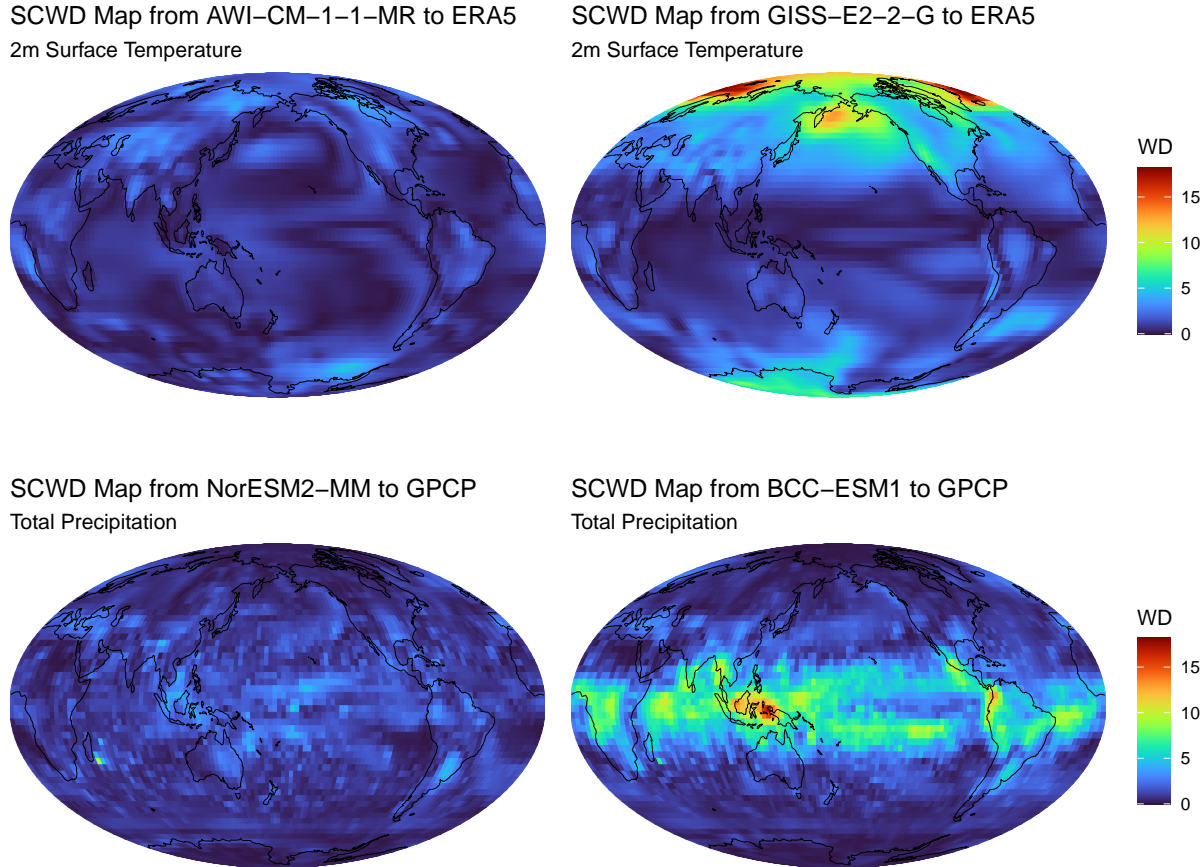


Figure 3. Top: Map of local Wasserstein distances from ERA5 to two CMIP6 2m surface temperature outputs: AWI-CM-1-1-MR and GISS-E2-2-G. Bottom: Map of local Wasserstein distances from GPCP to two CMIP6 total precipitation outputs: NorESM2-MM and BCC-ESM1. Color fill at each location is determined by the WD between the local distributions obtained from the convolution slicer in Definition 3.4. The color scale is shared for both maps and continental boundaries are included in black to aid spatial comparisons.

common in CMIP models, in which excessive precipitation is produced in the southern tropics (Mechoso et al., 1995). This trend is much more pronounced for BCC-ESM1 than for NorESM2-MM. Additionally, BCC-ESM1 has a region of particularly high WD values around eastern Indonesia, where wind-terrain interaction plays an important role in the regional distribution of precipitation. This region has been previously highlighted in Zhang et al. (2021) as an area where BCC-ESM1 heavily overestimates annual mean precipitation.

4.3. Comparing CMIP5 and CMIP6

Figure 4 provides the SCWD calculations for each CMIP model and NCEP to the ERA5 Reanalysis. Between the two CMIP eras, the median SCWD value for CMIP6 models to ERA5 is lower than that of CMIP5. However, the two boxplots are overall very similar, so the difference between the CMIP5 and CMIP6 ensembles is subtle. In addition, the model with the highest SCWD to ERA5 comes from

the CMIP6 ensemble. Overall, we see a promising, albeit limited, decrease in SCWD for general CMIP6 models compared to CMIP5. This indicates improved performance of CMIP6 when it comes to reconstructing realistic temperature distributions at the local level.

Figure 5 provides the SCWD calculations for each CMIP model and ERA5/NCEP to the GPCP observations. Between the two CMIP phases, the median SCWD value for CMIP6 is again lower than that of CMIP5. Compared to the surface temperature boxplots in Figure 4, the difference between CMIP5 and CMIP6 is even more distinct. This indicates that relative to surface temperature, precipitation modeling has seen greater gains with the transition from CMIP5 to CMIP6. The improvement of the CMIP6 models compared to CMIP5 in precipitation representation has been reported in some previous studies using different evaluation methods (e.g., Chen et al. (2021)). It can be probably attributed to the more advanced model physics and overall higher model resolution in CMIP6.

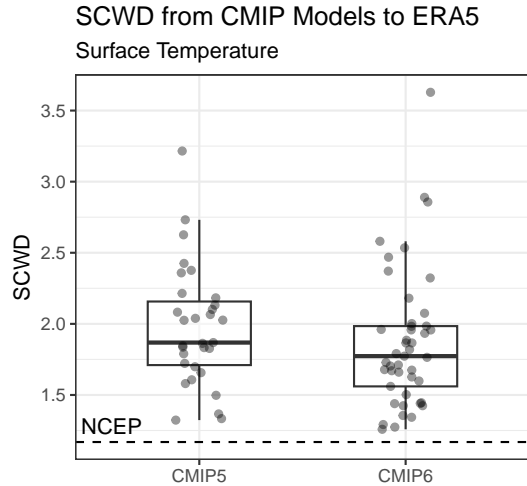


Figure 4. Boxplots of SCWD from the CMIP5 and CMIP6 model outputs to the ERA5 Reanalysis for 2m surface temperature. Each point represents the SCWD value for one climate model output to ERA5, with CMIP5 and CMIP6 separated into two boxplots for comparison. A dashed line is included to represent the SCWD from the NCEP Reanalysis to ERA5.

4.4. Metric Comparison

We compare our method to a previous climate model validation approach and assess our choice of range parameter by generating three additional rankings for the CMIP model outputs: SCWD with a range of 500km and 2,500km respectively, and the global mean-based WD from Vissio et al. (2020). These rankings can be seen alongside our original 1,000km SCWD results in Appendix D. Here, we focus on the CMIP6 results in Table 2 in the Appendix.

Overall, the SCWD rankings are nearly identical regardless of the range parameter. The only exception is for a few total precipitation models, such as GFDL-CM4 and E3SM-2-0, which see improvement in the rankings for higher range parameters. However, there is a larger discrepancy between the rankings for SCWD with 1,000km range and the global mean-based WD (GMWD). For surface temperature, even though the SCWD from NCEP to ERA5 is lower than that of all CMIP6 models, the GMWD ranks NCEP among the median CMIP6 models. For total precipitation, we see a similar result for ERA5 compared to GPCP: ERA5 has the best ranking when using SCWD but only an average ranking for GMWD. These results indicate that incorporating local perspectives, rather than just the global mean, leads to a distance that is more skilled at determining similarities between climate models and observational datasets. More specifically, a model that represents the global mean well may have large compensating errors at the regional scale. SCWD can better represent the regional performance of climate models than GMWD and the individual slices provide more information about where a model excels or struggles.

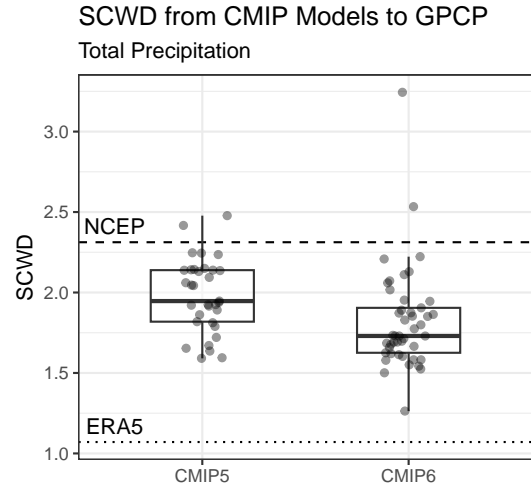


Figure 5. Boxplots of SCWD from the CMIP5 and CMIP6 model outputs to the GPCP observational dataset for total precipitation. Each point represents the SCWD value for one climate model output to GPCP, with CMIP5 and CMIP6 separated into two boxplots for comparison. Dotted and dashed lines are included to represent the SCWD from ERA5 and NCEP to GPCP, respectively.

5. Discussion and Future Work

Climate model validation is critical for ensuring that climate models faithfully represent the Earth system. To this end, we developed a new similarity measure, called spherical convolutional Wasserstein distance (SCWD), which quantifies model performance in a way that properly accounts for spatial variability. SCWD builds on previous sliced WD methods to compare distributions of infinite-dimensional functional data, specifically surfaces on the sphere \mathbb{S}^2 . We show improved performance over previous approaches for model evaluation: SCWD better recognizes the similarities between observed and reanalysis datasets relative to climate models. In addition, SCWD identifies regions where climate models deviate from observed conditions, providing useful insights to climate modelers.

Due to the shared spherical domain, SCWD could be directly applied to compare distributions of 360° images. In this case, a straightforward extension would allow for multiple convolution layers similar to the rectangular case in Nguyen & Ho (2022). SCWD could also be adapted to compare distributions of spatiotemporal fields, rather than spatial fields as in this article, by including both time and space in the functional data domain. This would require specifying a space-time kernel function (Porcu et al., 2016). The more general functional sliced WD framework has a variety of potential use cases for comparing distributions of functions on a broad class of manifolds. Potential application areas where the data lie on non-trivial manifolds include facial recognition (Li et al., 2014), astronomy (Szapudi, 2008), and ecology (Sutherland et al., 2015).

6. Acknowledgements

This research was partially supported by the National Science Foundation through awards DGE-1922758 and DMS-2124576.

7. Impact Statement

Climate models are the primary tool for climate prediction and projection. However, deficiencies persist among climate models despite decades of improvement. Our method offers a succinct yet informative approach to evaluating climate models against observational and reanalysis data, both on the global and regional scales. It provides valuable guidance for climate model improvement and can assist in selecting more reliable models to reduce uncertainty in climate projections, which is crucial for climate mitigation and adaptation efforts.

References

- Adler, R., Wang, J.-J., Sapiano, M., Huffman, G., Bolvin, D., Nelkin, E., et al. Global precipitation climatology project (gpcp) climate data record (cdr), version 1.3 (daily). 2020.
- Ayugi, B., Zhihong, J., Zhu, H., Ngoma, H., Babaoumail, H., Rizwan, K., and Dike, V. Comparison of cmip6 and cmip5 models in simulating mean and extreme precipitation over east africa. *International Journal of Climatology*, 41(15):6474–6496, 2021.
- Bengtsson, L., Hagemann, S., and Hodges, K. I. Can climate trends be calculated from reanalysis data? *Journal of Geophysical Research: Atmospheres*, 109(D11), 2004.
- Bonet, C., Berg, P., Courty, N., Septier, F., Drumetz, L., and Pham, M.-T. Spherical sliced-wasserstein. *arXiv preprint arXiv:2206.08780*, 2022.
- Bonneel, N., Rabin, J., Peyré, G., and Pfister, H. Sliced and radon wasserstein barycenters of measures. *Journal of Mathematical Imaging and Vision*, 51:22–45, 2015.
- Bugni, F. A. and Horowitz, J. L. Permutation tests for equality of distributions of functional data. *Journal of Applied Econometrics*, 36(7):861–877, 2021.
- Chen, C.-A., Hsu, H.-H., and Liang, H.-C. Evaluation and comparison of cmip6 and cmip5 model performance in simulating the seasonal extreme precipitation in the western north pacific and east asia. *Weather and Climate Extremes*, 31:100303, 2021.
- Cressie, N., Pavlicová, M., and Santner, T. J. Detecting signals in fmri data using powerful fdr procedures. *Statistics and its interface*, 1(1):23–32, 2008.
- Driscoll, J. R. and Healy, D. M. Computing fourier transforms and convolutions on the 2-sphere. *Advances in applied mathematics*, 15(2):202–250, 1994.
- Eyring, V., Bony, S., Meehl, G. A., Senior, C. A., Stevens, B., Stouffer, R. J., and Taylor, K. E. Overview of the coupled model intercomparison project phase 6 (cmip6) experimental design and organization. *Geoscientific Model Development*, 9(5):1937–1958, 2016. doi: 10.5194/gmd-9-1937-2016. URL <https://gmd.copernicus.org/articles/9/1937/2016/>.
- Flato, G., Marotzke, J., Abiodun, B., Braconnot, P., Chou, S. C., Collins, W., Cox, P., Driouech, F., Emori, S., Eyring, V., et al. Evaluation of climate models. In *Climate change 2013: the physical science basis. Contribution of Working Group I to the Fifth Assessment Report of the Intergovernmental Panel on Climate Change*, pp. 741–866. Cambridge University Press, 2014.
- Gijbels, I. and Nagy, S. On a general definition of depth for functional data. 2017.
- Hall, P. and Van Keilegom, I. Two-sample tests in functional data analysis starting from discrete data. *Statistica Sinica*, pp. 1511–1531, 2007.
- Harris, T., Li, B., Steiger, N. J., Smerdon, J. E., Narisetty, N., and Tucker, J. D. Evaluating proxy influence in assimilated paleoclimate reconstructions—testing the exchangeability of two ensembles of spatial processes. *Journal of the American Statistical Association*, 116(535):1100–1113, 2021.
- Heaton, M., Katzfuss, M., Berrett, C., and Nychka, D. Constructing valid spatial processes on the sphere using kernel convolutions. *Environmetrics*, 25(1):2–15, 2014.
- Hering, A. S. and Genton, M. G. Comparing spatial predictions. *Technometrics*, 53(4):414–425, 2011.
- Hersbach, H., Bell, B., Berrisford, P., Hirahara, S., Horányi, A., Muñoz-Sabater, J., Nicolas, J., Peubey, C., Radu, R., Schepers, D., et al. The era5 global reanalysis. *Quarterly Journal of the Royal Meteorological Society*, 146(730):1999–2049, 2020.
- Horváth, L., Kokoszka, P., and Reeder, R. Estimation of the mean of functional time series and a two-sample problem. *Journal of the Royal Statistical Society: Series B (Statistical Methodology)*, 75(1):103–122, 2013.
- Hubbert, S. and Jäger, J. Generalised wendland functions for the sphere. *Advances in Computational Mathematics*, 49(1):3, 2023.
- Huffman, G. J., Adler, R. F., Morrissey, M. M., Bolvin, D. T., Curtis, S., Joyce, R., McGavock, B., and Susskind,

- J. Global precipitation at one-degree daily resolution from multisatellite observations. *Journal of hydrometeorology*, 2(1):36–50, 2001.
- Janowiak, J. E., Gruber, A., Kondragunta, C., Livezey, R. E., and Huffman, G. J. A comparison of the ncep–ncar reanalysis precipitation and the gpcp rain gauge–satellite combined dataset with observational error considerations. *Journal of Climate*, 11(11):2960–2979, 1998.
- Kanamitsu, M., Ebisuzaki, W., Woollen, J., Yang, S.-K., Hnilo, J., Fiorino, M., and Potter, G. Ncep–doe amip–ii reanalysis (r-2). *Bulletin of the American Meteorological Society*, 83(11):1631–1644, 2002.
- Karim, R., Tan, G., Ayugi, B., Babausmail, H., and Liu, F. Evaluation of historical cmip6 model simulations of seasonal mean temperature over pakistan during 1970–2014. *Atmosphere*, 11(9):1005, 2020.
- Kelley, M., Schmidt, G. A., Nazarenko, L. S., Bauer, S. E., Ruedy, R., Russell, G. L., Ackerman, A. S., Aleinov, I., Bauer, M., Bleck, R., et al. Giss-e2. 1: Configurations and climatology. *Journal of Advances in Modeling Earth Systems*, 12(8):e2019MS002025, 2020.
- Kim, J. U. Invariant measures for a stochastic nonlinear schrödinger equation. *Indiana University mathematics journal*, pp. 687–717, 2006.
- Kolouri, S., Nadjahi, K., Simsekli, U., Badeau, R., and Rohde, G. Generalized sliced wasserstein distances. *Advances in neural information processing systems*, 32, 2019.
- Li, B. and Smerdon, J. E. Defining spatial comparison metrics for evaluation of paleoclimatic field reconstructions of the common era. *Environmetrics*, 23(5):394–406, 2012.
- Li, B., Zhang, X., and Smerdon, J. E. Comparison between spatio-temporal random processes and application to climate model data. *Environmetrics*, 27(5):267–279, 2016.
- Li, J., Huo, R., Chen, H., Zhao, Y., and Zhao, T. Comparative assessment and future prediction using cmip6 and cmip5 for annual precipitation and extreme precipitation simulation. *Frontiers in Earth Science*, 9, 2021. ISSN 2296-6463. doi: 10.3389/feart.2021.687976. URL <https://www.frontiersin.org/article/10.3389/feart.2021.687976>.
- Li, R., Turaga, P., Srivastava, A., and Chellappa, R. Differential geometric representations and algorithms for some pattern recognition and computer vision problems. *Pattern Recognition Letters*, 43:3–16, 2014.
- Li, T. and Ma, J. Functional data clustering analysis via the learning of gaussian processes with wasserstein distance. In *Neural Information Processing: 27th International Conference, ICONIP 2020, Bangkok, Thailand, November 23–27, 2020, Proceedings, Part II 27*, pp. 393–403. Springer, 2020.
- Lund, R. and Li, B. Revisiting climate region definitions via clustering. *Journal of Climate*, 22(7):1787–1800, 2009.
- Mechoso, C. R., Robertson, A. W., Barth, N., Davey, M., Delecluse, P., Gent, P., Ineson, S., Kirtman, B., Latif, M., Le Treut, H., et al. The seasonal cycle over the tropical pacific in coupled ocean–atmosphere general circulation models. *Monthly Weather Review*, 123(9):2825–2838, 1995.
- Nguyen, K. and Ho, N. Revisiting sliced wasserstein on images: From vectorization to convolution. *Advances in Neural Information Processing Systems*, 35:17788–17801, 2022.
- Nychka, D., Bandyopadhyay, S., Hammerling, D., Lindgren, F., and Sain, S. A multiresolution gaussian process model for the analysis of large spatial datasets. *Journal of Computational and Graphical Statistics*, 24(2):579–599, 2015.
- Pomann, G.-M., Staicu, A.-M., and Ghosh, S. A two sample distribution-free test for functional data with application to a diffusion tensor imaging study of multiple sclerosis. *Journal of the Royal Statistical Society. Series C, Applied Statistics*, 65(3):395, 2016.
- Porcu, E., Bevilacqua, M., and Genton, M. G. Spatio-temporal covariance and cross-covariance functions of the great circle distance on a sphere. *Journal of the American Statistical Association*, 111(514):888–898, 2016.
- Räaisaänen, J. How reliable are climate models? *Tellus A: Dynamic Meteorology and Oceanography*, 59(1):2–29, 2007.
- Roca, R., Haddad, Z. S., Akimoto, F. F., Alexander, L., Behrangi, A., Huffman, G., Kato, S., Kidd, C., Kirstetter, P.-E., Kubota, T., et al. The joint ipwg/gewex precipitation assessment, 2021.
- Rood, R. B. *Validation of Climate Models: An Essential Practice*, pp. 737–762. Springer International Publishing, Cham, 2019. ISBN 978-3-319-70766-2. doi: 10.1007/978-3-319-70766-2_30. URL https://doi.org/10.1007/978-3-319-70766-2_30.
- Shen, X., Huang, H.-C., and Cressie, N. Nonparametric hypothesis testing for a spatial signal. *Journal of the American Statistical Association*, 97(460):1122–1140, 2002.

- Staicu, A.-M., Li, Y., Crainiceanu, C. M., and Ruppert, D. Likelihood ratio tests for dependent data with applications to longitudinal and functional data analysis. *Scandinavian Journal of Statistics*, 41(4):932–949, 2014.
- Stein, E. M. and Shakarchi, R. *Functional analysis: introduction to further topics in analysis*, volume 4. Princeton University Press, 2011.
- Sutherland, C., Fuller, A. K., and Royle, J. A. Modelling non-euclidean movement and landscape connectivity in highly structured ecological networks. *Methods in Ecology and Evolution*, 6(2):169–177, 2015.
- Szapudi, I. Introduction to higher order spatial statistics in cosmology. In *Data Analysis in Cosmology*, pp. 457–492. Springer, 2008.
- Tapiador, F., Navarro, A., Levizzani, V., García-Ortega, E., Huffman, G., Kidd, C., Kucera, P., Kummerow, C., Masunaga, H., Petersen, W., et al. Global precipitation measurements for validating climate models. *Atmospheric Research*, 197:1–20, 2017.
- Vallender, S. Calculation of the wasserstein distance between probability distributions on the line. *Theory of Probability & Its Applications*, 18(4):784–786, 1974.
- Villani, C. and Villani, C. The wasserstein distances. *Optimal Transport: Old and New*, pp. 93–111, 2009.
- Vissio, G., Lembo, V., Lucarini, V., and Ghil, M. Evaluating the performance of climate models based on wasserstein distance. *Geophysical Research Letters*, 47(21): e2020GL089385, 2020.
- Wang, J.-L., Chiou, J.-M., and Müller, H.-G. Functional data analysis. *Annual Review of Statistics and its application*, 3:257–295, 2016.
- Washington, W. M. and Parkinson, C. *Introduction to three-dimensional climate modeling*. University science books, 2005.
- Yun, S., Zhang, X., and Li, B. Detection of local differences in spatial characteristics between two spatiotemporal random fields. *Journal of the American Statistical Association*, 117(537):291–306, 2022.
- Zamani, Y., Hashemi Monfared, S. A., Hamidianpour, M., et al. A comparison of cmip6 and cmip5 projections for precipitation to observational data: the case of northeastern iran. *Theoretical and Applied Climatology*, 142(3): 1613–1623, 2020.
- Zhang, J., Wu, T., Zhang, F., Furtado, K., Xin, X., Shi, X., Li, J., Chu, M., Zhang, L., Liu, Q., et al. Bcc-esm1 model datasets for the cmip6 aerosol chemistry model intercomparison project (aerchemmip). *Advances in Atmospheric Sciences*, 38:317–328, 2021.
- Zhang, J.-T. and Chen, J. Statistical inferences for functional data. 2007.
- Zhang, X. and Shao, X. Two sample inference for the second-order property of temporally dependent functional data. 2015.
- Zhao, S., He, W., Dong, T., Zhou, J., Xie, X., Mei, Y., Wan, S., and Jiang, Y. Evaluation of the performance of cmip5 models to simulate land surface air temperature based on long-range correlation. *Frontiers in Environmental Science*, pp. 6, 2021.

A. Proof of Theorem 3.3

Proof. Let $r \geq 1$, let \mathcal{S} be a compact subset of \mathbb{R}^n , and let $P, Q, U \in \mathcal{P}(L^2(\mathcal{S}))$. We show the identity property holds:

$$\begin{aligned} FSW_r(P, P) &= \left(\int_{\mathcal{S}} W_r(c_s \# P, c_s \# P)^r ds \right)^{1/r} \\ &= \left(\int_{\mathcal{S}} 0^r ds \right)^{1/r} \\ &= 0 \end{aligned}$$

The second line holds by the identity property of the ordinary WD. Next, the symmetry property:

$$\begin{aligned} FSW_r(P, Q) &= \left(\int_{\mathcal{S}} W_r(c_s \# P, c_s \# Q)^r ds \right)^{1/r} \\ &= \left(\int_{\mathcal{S}} W_r(c_s \# Q, c_s \# P)^r ds \right)^{1/r} \\ &= FSW_r(Q, P) \end{aligned}$$

The second line holds by the symmetry property of the ordinary WD. Next, the triangle inequality:

$$\begin{aligned} FSW_r(P, U) &= \left(\int_{\mathcal{S}} W_r(c_s \# P, c_s \# U)^r ds \right)^{1/r} \\ &\leq \left(\int_{\mathcal{S}} [W_r(c_s \# P, c_s \# Q) + W_r(c_s \# Q, c_s \# U)]^r ds \right)^{1/r} \\ &\leq \left(\int_{\mathcal{S}} W_r(c_s \# P, c_s \# Q)^r ds \right)^{1/r} + \left(\int_{\mathcal{S}} W_r(c_s \# Q, c_s \# U)^r ds \right)^{1/r} \\ &= FSW_r(P, Q) + FSW_r(Q, U) \end{aligned}$$

The second line holds by the triangle inequality property of the ordinary WD and the third line holds by the Minkowski inequality. Lastly, we check the r -convexity property. Let $\lambda \in [0, 1]$. If we take P as the reference distribution, this property tells us what happens to the functional sliced WD as we interpolate between Q and U :

$$\begin{aligned} FSW_r(P, \lambda Q + (1 - \lambda)U) &= \left(\int_{\mathcal{S}} W_r(c_s \# P, c_s \# [\lambda Q + (1 - \lambda)U])^r ds \right)^{1/r} \\ &= \left(\int_{\mathcal{S}} W_r(c_s \# P, \lambda c_s \# Q + (1 - \lambda)c_s \# U)^r ds \right)^{1/r} \\ &\leq \left(\int_{\mathcal{S}} \lambda W_r(c_s \# P, c_s \# Q)^r + (1 - \lambda) W_r(c_s \# P, c_s \# U)^r ds \right)^{1/r} \\ &\leq \left(\lambda \int_{\mathcal{S}} W_r(c_s \# P, \lambda c_s \# Q)^r ds \right)^{1/r} + \left((1 - \lambda) \int_{\mathcal{S}} W_r(c_s \# P, c_s \# U)^r ds \right)^{1/r} \\ &= \lambda^{1/r} FSW_r(P, Q) + (1 - \lambda)^{1/r} FSW_r(P, U) \end{aligned}$$

The second line follows from properties of linear operators (in this case c_s). The third line follows by the r -convexity of the ordinary WD, and the fourth line follows from the Minkowski inequality. We have shown all three pseudometric properties and the r -convexity property, so our proof is complete. \square

B. SCWD Implementation

The following algorithm describes the process by which we calculated the SCWD values shown in Section 4.

Algorithm 1 Spherical Convolutional Wasserstein Distance Approximation

DATA

Reference dataset $X_0(t), t \in \mathcal{T}_0$: sample of spatial fields

Model outputs $X_1(t), t \in \mathcal{T}_1, \dots, X_n(t), t \in \mathcal{T}_n$: n samples of spatial fields to be compared to X_0

PARAMETERS AND APPROXIMATION GRIDS

Wasserstein order parameter r : 2

Range parameter l : 1,000 km kernel radius

Approximation quantiles Q : 200 evenly spaced quantiles ranging from 0 to 1 with a step size of 0.005

Grid G_1 : 60×120 regular latitude-longitude grid of center points for strided convolution

Grid G_2 : 361×720 regular latitude-longitude grid to provide discrete approximation of spherical domain

STEP 1. PRECOMPUTE SLICING WEIGHTS

for each location $s \in G_1$ **do**

 Calculate vector of chordal distances from s to all locations in G_2

 Calculate Wendland function (3) with range l for all locations in G_2 using distance vector

 Apply area weighting to the Wendland kernel values using the area of each grid cell in G_2

 Normalize area-weighted kernel and store the results as a sparse vector $W(s)$

end for

STEP 2. COMPUTE SLICED QUANTILES

for $i \in 0, 1, \dots, n$ **do**

 Re-grid X_i to G_2 without smoothing (one nearest neighbor upsampling)

for each location $s \in G_1$ **do**

 Slice X_i into one dimension using the dot product $X_i^*(s, t) = \langle W(s), X_i(t) \rangle$

 Calculate the sliced quantile function of $X_i^*(s, t)$, denoted as $F_i^{-1}(s, q), q \in Q$

end for

end for

STEP 3. CALCULATE APPROXIMATE SCWD

for $i \in 1, \dots, n$ **do**

for each location $s \in G_1$ **do**

 Calculate the local WD between X_0 and X_i centered around s as $d_i(s)^r = \sum_{q \in Q} |F_0^{-1}(q) - F_i^{-1}(q)|^r$

end for

 Calculate the approximate SCWD between X_0 and X_i as $SCWD(X_0, X_i) \approx (\sum_{s \in G_1} d_i(s)^r)^{1/r}$

end for

The climate model outputs and reanalysis datasets (ERA, NCEP) used in our analysis have no missing data. However, the GPCP observational dataset used as the reference for total precipitation did have missing data at some sites for a few days in the historical period. To handle missing data in the GPCP dataset, we modified the slicing process in Step 2. If locations corresponding to greater than 50% of the convolution weight were missing when calculating a slice value, an NA value was recorded. The local WD calculations in Step 3 were computed ignoring these NA values. In total, 17,943 slices were missing sufficient data when using the 50% threshold. However, a total of 24,105,600 slices were considered for the GPCP dataset (3,348 days in the analysis period with 7,200 slices per day in the strided convolution), so the missing slices constituted under 0.1% of the final sliced GPCP data used in the analysis.

C. Table of Data Details and Access Links

Obs./Reanalysis Data	Longs	Lats	TAS	PR	CMIP6 Models	Longs	Lats	TAS	PR
NCEP Reanalysis	144	73	Yes	Yes	ACCESS-CM2	192	144	Yes	Yes
ERA5 Reanalysis	1440	721	Yes	Yes	ACCESS-ESM1-5	192	145	Yes	Yes
GPCP Observations	360	180	No	Yes	AWI-CM-1-1-MR	384	192	Yes	Yes
					AWI-ESM-1-1-LR	192	96	Yes	Yes
					BCC-ESM1	128	64	Yes	Yes
					CESM2	288	192	Yes	Yes
					CESM2-FV2	144	96	Yes	Yes
					CESM2-WACCM	288	192	Yes	Yes
					CESM2-WACCM-FV2	144	96	Yes	Yes
					CMCC-CM2-HR4	288	192	Yes	Yes
					CMCC-CM2-SR5	288	192	Yes	Yes
					CMCC-ESM2	288	192	Yes	Yes
					CanESM5	128	64	Yes	Yes
					E3SM-1-0	360	180	Yes	Yes
					E3SM-2-0	360	180	Yes	Yes
					E3SM-2-0-NARRM	360	180	Yes	Yes
					EC-Earth3	512	256	Yes	Yes
					EC-Earth3-AerChem	512	256	Yes	Yes
					EC-Earth3-CC	512	256	Yes	Yes
					EC-Earth3-Veg	512	256	Yes	Yes
					EC-Earth3-Veg-LR	320	160	Yes	Yes
					FGOALS-f3-L	288	180	Yes	Yes
					FGOALS-g3	180	80	Yes	Yes
					GFDL-CM4	288	180	Yes	Yes
					GFDL-ESM4	288	180	Yes	Yes
					GISS-E2-2-G	144	90	Yes	Yes
					ICON-ESM-LR*	N/A	N/A	Yes	Yes
					IITM-ESM	192	94	Yes	Yes
					INM-CM4-8	180	120	Yes	Yes
					INM-CM5-0	180	120	Yes	Yes
					IPSL-CM5A2-INCA	96	96	Yes	Yes
					IPSL-CM6A-LR	144	143	Yes	Yes
					IPSL-CM6A-LR-INCA	144	143	No	Yes
					KACE-1-0-G	192	144	Yes	Yes
					KIOST-ESM	192	96	Yes	Yes
					MIROC6	256	128	Yes	Yes
					MPI-ESM-1-2-HAM	192	96	Yes	Yes
					MPI-ESM1-2-HR	384	192	Yes	Yes
					MPI-ESM1-2-LR	192	96	Yes	Yes
					MRI-ESM2-0	320	160	Yes	Yes
					NESM3	192	96	Yes	Yes
					NorCPM1	144	96	Yes	Yes
					NorESM2-LM	144	96	Yes	Yes
					NorESM2-MM	288	192	Yes	Yes
					SAM0-UNICON	288	192	Yes	Yes
					TaiESM1	288	192	Yes	Yes

Table 1. Additional details for each observed/reanalysis data product and CMIP model output. The columns give the model name, longitude and latitude resolution, and availability of (2m) surface temperature (TAS) and total precipitation (PR) for each dataset. All datasets were obtained on a rectangular grid except ICON-ESM-LR, which was obtained on an icosahedral grid with 10,242 total cells.

CMIP5 and CMIP6 outputs: <https://esgf-node.llnl.gov/projects/esgf-llnl/>

ERA5 hourly data on single levels from 1940 to present: <https://cds.climate.copernicus.eu/cdsapp#!/dataset/reanalysis-era5-single-levels?tab=overview>

NCEP/DOE Reanalysis II: <https://psl.noaa.gov/data/gridded/data.ncep.reanalysis2.html>.

GPCP 1 Degree Daily Precipitation Estimate: <https://www.ncei.noaa.gov/products/climate-data-records/precipitation-gpcp-daily>.

D. Full SCWD Rankings and Metric Comparison

CMIP6 Surface Temperature Rankings

	SCWD (500km)	SCWD (1000km)	SCWD (2500km)	GMWD
NCEP Reanalysis	1.412	1.197	0.923	0.308
AWI-CM-1-1-MR	1.382	1.277	1.044	0.308
MPI-ESM1-2-HR	1.404	1.294	1.039	0.389
CESM2-WACCM	1.419	1.311	1.074	0.277
NorESM2-MM	1.476	1.363	1.121	0.095
CESM2	1.476	1.373	1.149	0.449
GFDL-ESM4	1.544	1.443	1.196	0.377
MPI-ESM1-2-LR	1.600	1.450	1.117	0.070
CMCC-CM2-HR4	1.561	1.459	1.228	0.722
AWI-ESM-1-1-LR	1.614	1.464	1.150	0.476
MRI-ESM2-0	1.581	1.467	1.198	0.161
CESM2-WACCM-FV2	1.679	1.526	1.246	0.452
CESM2-FV2	1.734	1.584	1.296	0.331
NorESM2-LM	1.774	1.622	1.341	0.645
ACCESS-ESM1-5	1.816	1.652	1.365	0.767
TaiESM1	1.797	1.680	1.443	0.141
E3SM-1-0	1.797	1.689	1.456	0.182
CMCC-ESM2	1.802	1.694	1.455	0.592
IPSL-CM6A-LR	1.803	1.697	1.458	0.557
GFDL-CM4	1.806	1.725	1.552	1.008
INM-CM5-0	1.937	1.736	1.364	0.435
IPSL-CM5A2-INCA	1.895	1.752	1.450	0.446
KACE-1-0-G	1.960	1.791	1.499	0.269
CMCC-CM2-SR5	1.896	1.791	1.559	0.702
MPI-ESM-1-2-HAM	1.949	1.814	1.521	0.174
ACCESS-CM2	1.964	1.840	1.597	0.092
EC-Earth3-Veg	1.943	1.877	1.737	0.475
NESM3	2.011	1.887	1.623	0.133
CanESM5	2.104	1.913	1.567	0.265
EC-Earth3-AerChem	2.016	1.946	1.795	0.207
EC-Earth3-Veg-LR	2.051	1.971	1.817	0.150
E3SM-2-0	2.072	1.973	1.775	0.541
SAM0-UNICON	2.091	1.980	1.747	0.744
E3SM-2-0-NARRM	2.087	1.997	1.815	0.658
FGOALS-f3-L	2.119	2.004	1.751	0.614
INM-CM4-8	2.236	2.035	1.629	0.252
EC-Earth3	2.156	2.087	1.939	0.238
EC-Earth3-CC	2.254	2.192	2.054	0.842
KIOST-ESM	2.430	2.338	2.139	0.631
ICON-ESM-LR	2.519	2.396	2.010	0.489
NorCPM1	2.638	2.492	2.195	1.218
BCC-ESM1	2.774	2.566	2.212	0.905
FGOALS-g3	2.738	2.603	2.325	0.695
MIROC6	3.006	2.878	2.611	1.531
IITM-ESM	2.996	2.905	2.709	0.692
GISS-E2-2-G	3.726	3.644	3.432	1.832

CMIP6 Total Precipitation Rankings

	SCWD (500km)	SCWD (1000km)	SCWD (2500km)	GMWD
ERA5 Reanalysis	1.804	1.133	0.701	0.252
NorESM2-MM	1.905	1.335	0.762	0.167
EC-Earth3	2.028	1.589	0.968	0.236
CESM2	2.425	1.597	0.891	0.263
EC-Earth3-CC	2.043	1.613	0.998	0.275
CESM2-WACCM	2.399	1.640	0.889	0.246
EC-Earth3-Veg	2.083	1.646	1.009	0.249
EC-Earth3-Veg-LR	2.080	1.647	1.006	0.193
EC-Earth3-AerChem	2.120	1.668	1.031	0.241
MIROC6	2.592	1.683	0.946	0.486
NorESM2-LM	2.137	1.686	0.972	0.182
CESM2-FV2	2.134	1.690	1.014	0.265
TaiESM1	2.593	1.723	1.028	0.384
MRI-ESM2-0	2.453	1.749	1.044	0.304
CESM2-WACCM-FV2	2.199	1.750	1.037	0.262
KACE-1-0-G	2.789	1.759	1.044	0.340
MPI-ESM1-2-HR	2.288	1.760	1.040	0.215
CMCC-ESM2	2.602	1.787	1.073	0.402
ACCESS-CM2	2.816	1.796	1.062	0.447
E3SM-1-0	2.432	1.800	1.055	0.359
AWI-CM-1-1-MR	2.327	1.802	1.074	0.234
CMCC-CM2-SR5	2.578	1.818	1.115	0.412
CMCC-CM2-HR4	2.601	1.818	1.112	0.291
GFDL-CM4	3.064	1.836	0.917	0.225
MPI-ESM1-2-LR	2.353	1.851	1.093	0.167
E3SM-2-0	3.042	1.861	0.967	0.276
E3SM-2-0-NARRM	3.120	1.873	0.953	0.276
IPSL-CM6A-LR	2.845	1.895	1.143	0.345
IPSL-CM6A-LR-INCA	2.926	1.952	1.163	0.349
IITM-ESM	2.616	1.964	1.177	0.240
NESM3	2.446	1.967	1.196	0.181
GFDL-ESM4	3.194	1.970	1.008	0.271
INM-CM5-0	2.973	1.971	1.207	0.359
ACCESS-ESM1-5	2.827	1.979	1.158	0.546
NorCPM1	2.469	1.980	1.233	0.080
SAM0-UNICON	3.064	1.984	1.066	0.332
INM-CM4-8	2.658	2.027	1.333	0.368
CanESM5	3.303	2.088	1.123	0.209
MPI-ESM-1-2-HAM	2.681	2.144	1.294	0.238
FGOALS-g3	3.438	2.157	1.136	0.097
KIOST-ESM	3.008	2.190	1.239	0.091
GISS-E2-2-G	2.847	2.201	1.366	0.152
AWI-ESM-1-1-LR	2.745	2.214	1.349	0.160
ICON-ESM-LR	2.849	2.295	1.413	0.118
IPSL-CM5A2-INCA	2.996	2.321	1.380	0.143
NCEP Reanalysis	3.738	2.490	1.289	0.581
FGOALS-f3-L	4.614	2.752	1.264	0.191
BCC-ESM1	4.575	3.458	1.491	0.110

Table 2. CMIP6 model rankings for both (2m) surface temperature and total precipitation based on similarity to the ERA5 Reanalysis (surface temperature) and GPCP observations (total precipitation). Distances are calculated using our proposed spherical convolutional WD (SCWD) as well as the global mean-based WD (GMWD) from Vissio et al. (2020). For the SCWD calculations, three different range parameters are chosen for the Wendland kernel: 500km, 1000km (our proposed choice), and 2500km. Color fill is unique to each column in the tables, and is calculated using ranks.

CMIP5 Surface Temperature Rankings

	SCWD (500km)	SCWD (1000km)	SCWD (2500km)	GMWD
NCEP Reanalysis	1.412	1.197	0.923	0.308
MPI-ESM-P	1.491	1.347	1.039	0.157
MPI-ESM-MR	1.491	1.356	1.070	0.292
MPI-ESM-LR	1.530	1.390	1.089	0.132
MIROC4h	1.620	1.516	1.292	0.648
ACCESS1-3	1.807	1.612	1.238	0.209
NorESM1-M	1.816	1.634	1.310	0.485
ACCESS1-0	1.848	1.683	1.385	0.055
IPSL-CM5A-MR	1.833	1.719	1.448	0.307
GFDL-CM3	1.877	1.745	1.446	0.371
HadGEM2-AO	1.977	1.815	1.516	0.305
EC-EARTH	1.921	1.841	1.650	0.862
HadGEM2-ES	2.014	1.857	1.582	0.336
CMCC-CMS	1.984	1.865	1.617	0.157
MIROC-ESM-CHEM	2.118	1.870	1.528	0.322
CNRM-CM5	2.018	1.891	1.618	0.303
MIROC-ESM	2.141	1.896	1.559	0.276
GFDL-ESM2M	2.203	2.049	1.763	0.192
CanESM2	2.267	2.057	1.703	0.265
IPSL-CM5A-LR	2.181	2.059	1.805	1.111
MRI-ESM1	2.187	2.084	1.848	0.108
CMCC-CM	2.197	2.100	1.861	0.273
MRI-CGCM3	2.224	2.120	1.881	0.167
GFDL-ESM2G	2.309	2.155	1.868	0.348
HadGEM2-CC	2.350	2.205	1.950	0.628
MIROC5	2.357	2.235	1.972	0.855
CMCC-CESM	2.614	2.389	2.088	0.147
HadCM3	2.575	2.402	2.111	0.602
inmcm4	2.623	2.453	2.101	0.381
FGOALS-s2	2.877	2.662	2.253	1.034
CSIRO-Mk3-6-0	2.961	2.763	2.393	0.977
FGOALS-g2	3.186	3.000	2.703	1.680
IPSL-CM5B-LR	3.361	3.238	2.929	0.626

CMIP5 Total Precipitation Rankings

	SCWD (500km)	SCWD (1000km)	SCWD (2500km)	GMWD
ERA5 Reanalysis	1.804	1.133	0.701	0.252
ACCESS1-0	2.257	1.665	1.033	0.410
HadGEM2-ES	2.274	1.668	1.039	0.394
HadGEM2-CC	2.337	1.713	1.058	0.364
HadGEM2-AO	2.387	1.733	1.067	0.428
MIROC5	2.380	1.752	1.082	0.533
MIROC4h	2.809	1.817	1.080	0.278
EC-EARTH	2.334	1.859	1.156	0.199
ACCESS1-3	2.642	1.913	1.146	0.487
FGOALS-g2	2.774	1.913	1.109	0.132
NorESM1-M	2.435	1.937	1.212	0.147
CanESM2	2.767	1.989	1.185	0.107
CMCC-CMS	2.498	2.002	1.214	0.251
MPI-ESM-LR	2.527	2.009	1.169	0.275
GFDL-CM3	2.695	2.011	1.194	0.319
HadCM3	2.550	2.027	1.266	0.234
CanCM4	2.855	2.028	1.188	0.111
CMCC-CM	3.011	2.049	1.156	0.227
CMCC-CESM	2.685	2.129	1.319	0.204
MPI-ESM-MR	2.652	2.129	1.253	0.331
MPI-ESM-P	2.686	2.148	1.255	0.265
IPSL-CM5A-MR	2.914	2.189	1.315	0.144
MIROC-ESM	2.727	2.211	1.399	0.134
MIROC-ESM-CHEM	2.749	2.230	1.417	0.118
IPSL-CM5A-LR	2.882	2.230	1.333	0.080
GFDL-ESM2G	2.971	2.242	1.353	0.309
MRI-CGCM3	3.590	2.276	1.248	0.237
GFDL-ESM2M	3.280	2.279	1.232	0.317
MRI-ESM1	3.698	2.288	1.243	0.257
CSIRO-Mk3-6-0	2.898	2.326	1.404	0.213
FGOALS-s2	3.199	2.367	1.342	0.086
CNRM-CM5	3.764	2.412	1.218	0.384
NCEP Reanalysis	3.738	2.490	1.289	0.581
inmcm4	3.151	2.570	1.621	0.481
IPSL-CM5B-LR	4.504	2.630	1.168	0.145

Table 3. CMIP5 model rankings for both (2m) surface temperature and total precipitation based on similarity to the ERA5 Reanalysis (surface temperature) and GPCP observations (total precipitation). Distances are calculated using our proposed spherical convolutional WD (SCWD) as well as the global mean-based WD (GMWD) from Vissio et al. (2020). For the SCWD calculations, three different range parameters are chosen for the Wendland kernel: 500km, 1000km (our proposed choice), and 2500km. Color fill is unique to each column in the tables, and is calculated using ranks.